

VLT/SINFONI Integral Field Spectroscopy of The Super-antennae^{*}

J. Reunanen¹, L. E. Tacconi-Garman², V. D. Ivanov³

¹*Leiden Observatory, PO Box 9513, 2300 RA Leiden, The Netherlands; reunanen@strw.leidenuniv.nl*

²*European Southern Observatory, Karl Schwarzschildstrasse 2, 85748 Garching, Germany; ltacconi@eso.org*

³*European Southern Observatory, Alonso de Cordova 3107, Santiago 19, Chile; vivanov@eso.org*

ABSTRACT

We present the results of H - and K -band VLT/SINFONI integral field spectroscopy of the ULIRG IRAS 19254–7245 (The Super-antennae), an interacting double galaxy system containing an embedded AGN. Deep K -band spectroscopy reveals $\text{Pa}\alpha$ arising in a warped disc with position angle of 330° and an inclination $i = 40 - 55^\circ$. The kinematic parameters derived for H_2 are similar to $\text{Pa}\alpha$. Two high-ionization emission lines, $[\text{Si VI}]$ and $[\text{Al IX}]$, are detected and we identify as $[\text{Ni II}]$ the line observed at $1.94 \mu\text{m}$. Diluting non-stellar continuum, which was previously detected, has decayed, and the H -band continuum emission is consistent with pure stellar emission. Based on H_2 emission line ratios it is likely that at the central 1-kpc region H_2 is excited by UV fluorescence in dense clouds while shock excitation is dominant further out. This scenario is supported by very low $\text{Pa}\alpha$ to H_2 line ratio detected outside the nuclear region and non-thermal ortho/para ratios ($\sim 2.0 - 2.5$) close to the nucleus.

Key words: galaxies: starburst – galaxies: Seyfert – galaxies: individual(The Super-antennae) – infrared: galaxies

1 INTRODUCTION

The Super-antennae (IRAS 19254–7245) at a redshift of $z \simeq 0.062$ (distance of ~ 260 Mpc assuming $H_0 = 71 \text{ km s}^{-1} \text{ Mpc}^{-1}$; Spergel et al. 2003) is an interacting double galaxy system where the two components are separated by $\sim 8''$ (~ 2 kpc). Visually the most notable feature of the system are the thin antennae extending up to $5'$ (~ 350 kpc), far longer than similar feature of the Antennae galaxy (~ 100 kpc).

The starburst activity powering the total infrared luminosity of $10^{11.91} L_{\text{IR}}/L_\odot$ (Duc, Mirabel & Maza 1997) in the system has been triggered by a 3 : 1 mass ratio encounter (Dasyra et al. 2006). The northern nucleus is less luminous than the southern nucleus in the infrared, and is believed to be in a post-starburst stage (e.g. Berta et al. 2003), while the southern galaxy is a starburst with an embedded AGN. Berta et al. (2003) found the spectrophotometric characteristics of the southern nuclei to be mostly consistent with two main stellar populations: an intermediate aged (1 Gy) starburst, which represents ~ 35 percent of the luminous mass of the galaxy and an old 12 Gy population representing the remaining ~ 65 percent of the total luminous mass. In addi-

tion, the southern nucleus has an intense ongoing starburst, which contributes little to the total luminous mass.

The evidence for the presence of an AGN comes from the optical emission line ratios (Mirabel, Lutz & Maza 1991), IR coronal-emission lines (Vanzi et al. 2002), observations of a hard, flat X-ray component above 2 keV (Pappa, Georgantopoulos & Stewart 2000), and strong Fe $K\alpha$ emission lines (Braitto et al. 2003) interpreted as a Compton-thick X-ray source. Like in other LIRGs/ULIRGs, a long-standing question has been whether the spectral energy distribution of the southern galaxy is dominated by the starburst or the AGN. The mid-IR spectroscopic diagnostics are intermediate between those for starbursts and AGN (Genzel et al. 1998). Recently, Charmandaris et al. (2002) and Risaliti et al. (2003; 2006) claimed the AGN is the main energy source in the southern galaxy based on mid-IR ISO and deep L -band ground-based spectroscopy, respectively.

Based on the integral field spectroscopic data obtained with VLT/SINFONI on the southern galaxy, we discuss the nuclear spectrum, excitation of molecular H_2 emission lines and the morphology and kinematic properties of ionized and molecular gas.

In addition to the high-excitation emission lines requiring the presence of either strong ionising continuum or fast shocks with $v_s \simeq 200 \text{ km s}^{-1}$ or greater (Contini & Viegas 2001), other AGN indicators in near-IR wavelength range

^{*} Based on observations collected at the European Southern Observatory, Paranal, Chile (60.A-9041(A)).

covered in this work are the variability of the emission lines and non-stellar continuum. Considering the distance and brightness of the Super-antennae, supernovae and their subsequent evolution are unlikely to produce detectable spectroscopic variability at the nucleus.

The dominant excitation mechanism for H_2 has been under debate for years, the two main candidates being UV fluorescence (e.g. Black & van Dishoeck 1987; Sternberg & Dalgarno 1989) and shocks (e.g. Hollenbach & McKee 1989). The interpretation of H_2 line ratios is complicated due to the strong dependence of line ratios on density; the energy levels are thermalised through inter-molecule collisions and the line ratios in dense clouds illuminated by intense UV radiation are very similar to those from purely thermal excitation, either through shocks or X-rays. Furthermore the H_2 line ratios are affected by the spin degeneracy of the levels. Radiative decay between ortho (odd J) and para (even J) is not possible due to different spin and in the ground electric state only $\Delta J = 0, \pm 2$ transitions are possible. For purely thermal excitation the ratio between the ortho and para levels is 3.0, but is lower for fluorescence in tenuous gas (~ 1.9 using the 1–0 S(1), S(2) and S(3) transitions; Black & van Dishoeck 1987).

As the Super-antennae is an interacting system, the kinematics is expected to be more complex than in the case of non-interacting galaxies. In the literature multiple gaussian have been used to approximate optical emission lines (Vanzi et al. 2002; Colina, Lipari & Macchetto 1991). Interpreting the results of multi-gaussian fits in a physically meaningful manner is however non-trivial, unless the components are clearly separated from each other. A more qualitative approach for tracing multiple velocity components is using the Gauss-Hermite series to describe the line profile (van der Marel & Franx 1993; Gerhard 1993). Strong kinematical components can also be revealed by fitting a warped disc model to the observed velocities.

The paper is organised as follows. In Section 2, the observations and data reduction are described. In Section 3 the results are presented and in Section 4 we summarise the conclusions of the work.

2 OBSERVATIONS AND DATA REDUCTION

The southern galaxy of the Super-antennae was observed during SINFONI (Spectrograph for INtegral Field Observations in the Near Infrared; Eisenhauer et al. 2003; Bonnet et al. 2004) Science Verification in Paranal, Chile, in August 2004 both in H ($R \simeq 2900$) and K bands ($R \simeq 4500$) with a 2048^2 pixel engineering grade detector. This engineering grade detector had two significant defects: a “glowcenter” at $2.38 \mu\text{m}$ and a large dead region at $>2.4 \mu\text{m}$. Unfortunately these artifacts compromised the data quality at the nucleus. The 250 mas pixel scale was used during the observations without Adaptive Optics providing a field of view (f.o.v) of $8'' \times 8''$. The total integration time was 14000 s in K and 1800 s in H -band. The average V -band seeing measured by the Differential Image Motion Monitor (DIMM) during the observations was $0''.94$ and $0''.77$ during the K -band and H -band observations, respectively, and the conditions were non-photometric. The observations were done

following the classical OSSO sequence of alternating object and sky exposures.

The data reduction was done with the *spread* software package (Schreiber et al. 2004) developed at the Max Planck Institut für Extraterrestrische Physik. The data were bad pixel and distortion corrected and sky subtracted using the nearest sky exposure. Instrumental flexure was tracked by cross-correlating the night sky OH emission lines before sky subtraction, and wavelength calibration was done by fitting a quadratic polynomial to Ne arc lamp frames for the K -band and Xe+Ar frames the H -band. Due to unstable conditions during the observations, the night sky emission lines and thermal background at the red end of the K band were not perfectly removed. This residual background was removed by calculating a median value along the edges of the cubes at each spectral plane and subtracting it. While this subtraction unavoidably removes faint continuum emission from the galaxy, the emission lines are unaffected as not even Pa α can be detected this far out and is not present in the subtracted spectra.

The relative wavelength shifts caused by the instrumental flexure between different exposures were determined by cross-correlation after collapsing the reconstructed data cubes. The cubes were combined and divided by the telluric standard spectra (Hip099481; B9.5V class star) in order to remove atmospheric signatures. Finally, the flux calibration was done by comparison with broad-band images (Vanzi et al. 2002). We estimate the absolute flux calibration is accurate to within 5–10 percent.

In order to enhance the signal-to-noise ratio of the images the data were smoothed with a $3 \text{ pixel} \times 3 \text{ pixel}$ boxcar ($0''.38 \times 0''.38$), which is much smaller than the resolution of the data. Emission line measurements were done automatically with scripts written by us for IRAF¹. If a detected line was significantly narrower than the instrumental profile, it was subtracted from the spectra and the fit was repeated. Finally, the detections were inspected and all obviously wrong fits due to cosmic ray residuals or noise were rejected. In the case of Pa α , which has multiple components that are difficult to fit automatically, the fit was carried over interactively within the central region. In all the images shown in later sections the lowest level displayed is at 2.5σ unless otherwise stated.

3 RESULTS

A broadband F804W image of the Super-antennae obtained from the HST data archive is presented in Fig. 1. The SINFONI field was centred on the southern nucleus and the field of view contains part of the bridge detected in broadband imaging connecting the two nuclei.

3.1 Nuclear spectrum

The nuclear spectrum of the Super-antennae is displayed in Fig. 2. In addition to Pa α fortuitously located at an at-

¹ IRAF is distributed by the National Optical Astronomy Observatories, which are operated by the Association of Universities for Research in Astronomy, Inc., under cooperative agreement with the National Science Foundation.

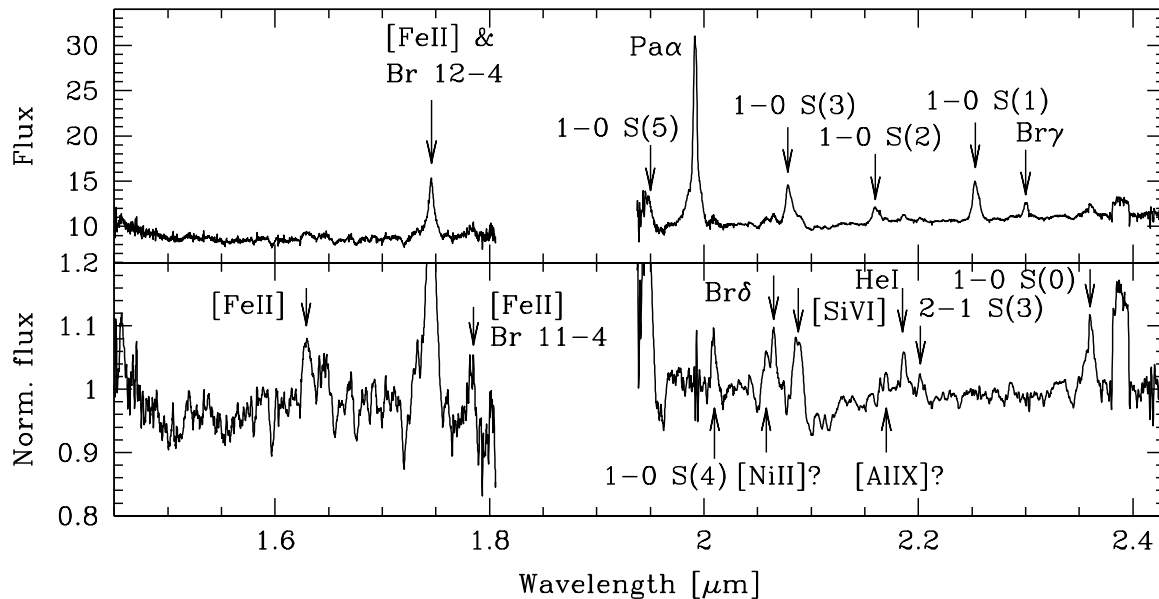


Figure 2. The summed spectrum of the central 5×5 spectra ($0''.6 \times 0''.6$) in units of $10^{-13} \text{ ergs cm}^{-1} \text{ s}^{-1} \mu\text{m}^{-1}$ with line identifications as indicated (*upper panel*). In the *lower panel* the normalised residuals after subtracting the strongest H α (Pa α , Br γ) and H $_2$ lines (1-0 S(1), S(2), S(3)) and smoothing with residual with five pixel boxcar are shown. The x-axis represents the observed wavelength.

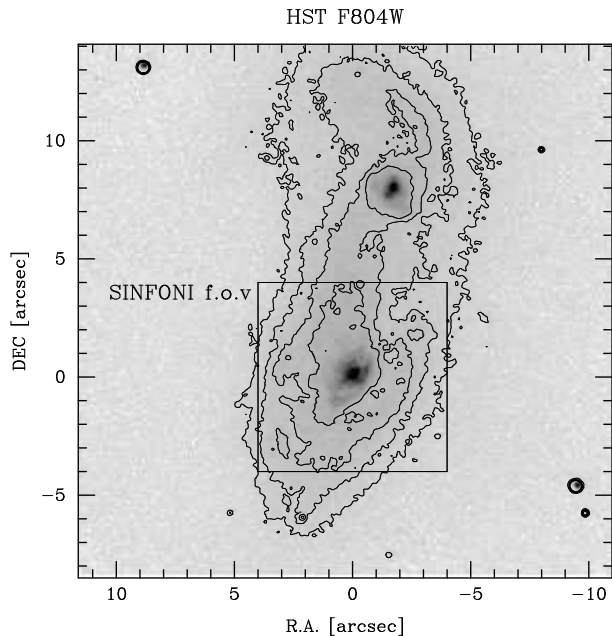


Figure 1. HST F804W filter image of the Super-antennae. The SINFONI field of view is indicated with a box. The antennae of the galaxy do not fit within the area depicted in this figure. East is left and north is up in this and any subsequent images.

mospherically relatively clean region at $\sim 2 \mu\text{m}$, the K -band spectrum shows many prominent molecular H $_2$ lines, hydrogen recombination lines Br γ and Br δ and He I $2.058 \mu\text{m}$. A careful study reveals also two coronal lines - [Si VI] $1.962 \mu\text{m}$ and [Al IX] $2.04 \mu\text{m}$ (redshifted to $2.0833 \mu\text{m}$ and $2.166 \mu\text{m}$, respectively). We have compared the observed fluxes to the

ones reported by Vanzani et al. (2002) in identical apertures. While the H $_2$ line ratios are in good agreement with Vanzani et al. (2002), the hydrogen recombination lines Br γ and Br δ are much weaker relative to H $_2$ lines. As the H $_2$ lines are unlikely to change in time scales of a few years, this variability in line ratios strongly suggests large fraction of the hydrogen recombination line luminosity in near-IR is due to AGN illuminated gas in NLR. The H $_2$ emission line fluxes are higher by ~ 40 percent than those reported by Vanzani et al. However, as discussed above, we were forced to use the broad-band images of Vanzani et al. for flux calibration, and it is possible that this difference can at least partly be attributed to changes in continuum brightness. This interpretation is likely, as the H -band CO absorption lines are less diluted by non-stellar continuum (Sect. 3.3) than detected by Vanzani et al. (2002).

A clear indication of an AGN in the Super-antennae is the presence of coronal emission lines: [Si VI] (ionisation energy 167 eV) previously detected by Vanzani et al. (2002) and a faint [Al IX] emission line (285 eV) detected at 12σ level. While [Al IX] has been detected only in few AGN (Maiolino et al. 1999; Reunanen et al. 2003), the line is one of the strongest NIR coronal lines when the ionising parameter (the ratio of hydrogen ionising photon to total hydrogen densities) is high enough. Detection of highly-ionised emission lines is not typical in ULIRGs; Murphy et al. (2001) found [Si VI] in only two galaxies out of 33 ULIRGs in their survey. This simply reflects the fact that stars are unable to photo-ionise the coronal emission lines, and the shocks in starforming regions are not likely excitation mechanism (e.g. Marconi et al. 1994; Rodríguez-Ardila et al. 2002).

An intriguing similarity between our nuclear spectrum and that presented in Vanzani et al. (2002) is the presence of a faint emission line at $2.058 \mu\text{m}$, which they attributed

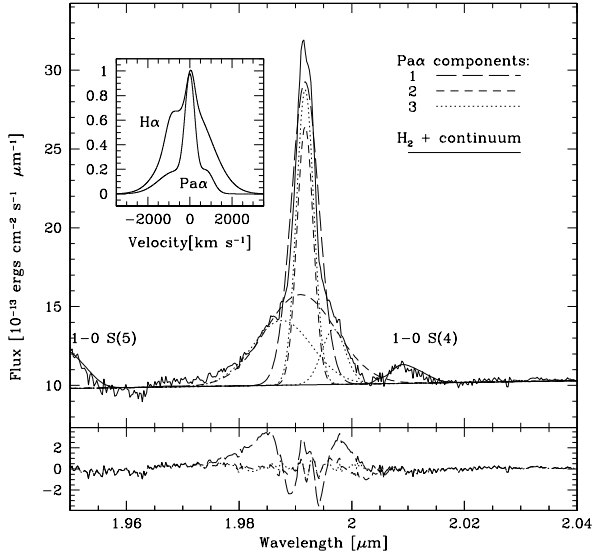


Figure 3. The Pa α spectrum summed over the central $0''.6 \times 0''.6$. In the upper panel the fits with one (*long-dashed*), two (*dashed*) and three Gaussians (*dotted*) are indicated as are the H $_2$ emission lines. In the lower panel the residuals of the fits are shown. The shape of the H $_2$ lines is taken from the isolated 1–0 S(1) line. The inset shows the comparison between the three component model of H α (Vanzi et al. 2002) and Pa α .

Table 1. Observed emission lines in the nucleus. Fluxes are given in units of 10^{-15} erg s $^{-1}$ cm $^{-2}$. [Fe II] 1.64 μ m is blended with Brackett 12–4 1.64117 μ m, [Fe II] 1.68 μ m with Brackett 11–4 1.68112 μ m and Br δ with H $_2$ 2–1 S(5) 1.94487 μ m.

Line	λ_0 Å	λ_{obs} Å	Flux	FWHM km s $^{-1}$
[Fe II]	15338.9	16314.3 \pm 1.4	1.09 \pm 0.06	1890 \pm 80
[Fe II]	16439.9	17457.3 \pm 0.4	5.10 \pm 0.07	1110 \pm 10
[Fe II]	16773.3	17826.4 \pm 3.0	1.24 \pm 0.10	1950 \pm 130
1–0 S(5)	18358.0	19472.2 \pm 3.1	2.64 \pm 0.4	1270 \pm 160
Pa α	18756.3	19909.8 \pm 0.2	13.30 \pm 0.04	515 \pm 2
1–0 S(4)	18919.7	20090.8 \pm 1.8	0.52 \pm 0.05	830 \pm 80
[Ni II]	19393.0	20586.9 \pm 2.2	0.16 \pm 0.04	550 \pm 110
Br δ	19451.0	20652.1 \pm 1.1	0.37 \pm 0.03	600 \pm 40
1–0 S(3)	19575.6	20798.2 \pm 0.3	3.34 \pm 0.03	920 \pm 10
[Si VI]	19634.1	20899.3 \pm 0.9	0.72 \pm 0.02	900 \pm 30
1–0 S(2)	20337.6	21609.2 \pm 0.3	1.20 \pm 0.02	1140 \pm 20
[Al IX]	20449.9	21695.6 \pm 1.3	0.12 \pm 0.01	450 \pm 50
He I	20586.9	21863.7 \pm 0.6	0.25 \pm 0.01	550 \pm 30
2–1 S(3)	20735.1	22020.4 \pm 1.1	0.13 \pm 0.02	500 \pm 50
1–0 S(1)	21218.3	22536.5 \pm 1.1	2.99 \pm 0.02	953 \pm 4
Br γ	21661.3	23002.3 \pm 0.6	0.66 \pm 0.02	540 \pm 20
1–0 S(0)	22233.0	23607.7 \pm 1.0	0.40 \pm 0.03	580 \pm 40

to night sky OH emission lines. However, the same feature is also present in our spectra which is otherwise free of telluric night sky signatures. The presence of several, relatively broad emission lines (2–1 S(5) 1.94487 μ m, Br δ 1.9451 μ m, 1–0 S(3) 1.95756 μ m, [Si VI] 1.96341 μ m) makes the study of the region complicated. In order to reduce the number of free parameters in the fit, we have assumed the line profiles of 1–0 S(3) and Br δ are identical to those of the isolated 1–0

S(1) and Pa α lines, respectively. Furthermore, we have used the 1–0 S(1) line profile for the 2–1 S(5) line fitting, keeping the position of the line fixed relative to 1–0 S(3) line. The addition of the 2–1 S(5) line, which is strongly blended with Br δ , is necessary to make the residuals around Br δ smaller. In typical starforming galaxies with 1–0 S(1)/Br γ \sim 1 (e.g. Goldader et al. 1997), the ratio 2–1 S(5) to Br δ is \sim 0.06 assuming thermal excitation with $T_{ex} = 2000$ K. However, due to the rather extreme 1–0 S(1)/Br γ ratio of \sim 5 observed in the Super-antennae, the contribution of 2–1 S(5) is \sim 30 percent of Br δ flux. The inclusion of 2–1 S(5) does not affect the position of the unidentified line. The fitting gives the wavelength for the unidentified line 2.0584 ± 0.0001 μ m ($\lambda_0 \simeq 1.937$ μ m). The best candidate in the NIST Atomic Spectra Database is [Ni II] 19393Å corresponding to the $3d^8 4s a^4F-3d^8 4s a^2F$ transition. Optical emission lines ($\lambda\lambda$ 7380 and 7414) originating from the same upper energy level have been detected in objects of various types, including nebulae (e.g. Osterbrock, Tran & Veilleux 1992), supernova remnants (e.g. Dennefeld 1986) and AGN (e.g. Halpern & Oke 1986). As the 1.93 μ m line should also be relatively strong (based on the relative A -values), the identification of this line as [Ni II] seems secure. The optical lines have, however, not been detected in the Super-antennae (Berta et al. 2003).

3.2 Emission line profiles

The most notable feature of the nuclear spectrum is of course Pa α . However, Pa α is badly fitted with a single Gaussian (Fig. 3). Similarly, multiple components (three or more; Vanzi et al. 2002; Colina, Lipari & Macchetto 1991) have been used to approximate the optical emission lines. The wavelength region (\sim 1.99 μ m) around Pa α appears to be completely free of atmospheric (telluric) residuals - redward of Pa α the strength, shape and position of 1–0 S(4) at 1.89 μ m is in excellent agreement with the measurements of the stronger and isolated 1–0 S(1) line. Therefore, the continuum level around Pa α line is very well determined. Pa α is asymmetric, with the blue wing being stronger, and is similar to the H α profile observed by Vanzi et al. While a two-component fit produces acceptable results in the sense that the residuals (red asymmetry) can be readily explained by obscured broad line region, the similarity with the H α suggests this is not the case. However, we note that the FWHM of the broader component in the two-component fit is similar to possible detection of broad H α in polarised emission by Pernechele et al. (2003).

When compared to H α , the center-most component in Pa α is much stronger and represents \sim 50 percent of the total Pa α emission, while the narrow ($\sigma = 185$ km s $^{-1}$) component of H α provides only 6.5 percent of the total line emission (Vanzi et al 2002). Qualitatively the weakness of coronal emission lines relative to the hydrogen recombination lines when compared with other Sy2 galaxies suggest the central component arises from a starburst and not from the NLR.

All the three main emission lines (Pa α , H $_2$ 1–0 S(1) and [Fe II]) have different line profiles. H $_2$ has a strong red component, while [Fe II] has a weak asymmetry to the red and is broad. Since [Fe II] has critical density of the order of $N_e \sim 10^4 - 10^5$ cm $^{-3}$ (Blietz et al. 1994), the BLR can-

not contribute significantly to the flux. Thus the shape of [Fe II] also supports multiple velocity components instead of a genuine broad component. Careful deblending also suggests that [Si VI] may be double-peaked, with a separation of $\sim 750 \text{ km s}^{-1}$ ($z = 0.06155, 0.06419$) between the two peaks, indicating it may originate from an unresolved disk. [Al IX] is too weak to determine whether the profile is similar to [Si VI].

3.3 Nuclear absorption lines

In addition to many prominent emission lines, the nuclear spectrum also contains several absorption lines, allowing the application of the penalised pixel fitting method (Cappellari & Emsellem 2004) to determine the line of sight velocity distribution. In this process, the line of sight velocity distribution is described by a Gauss-Hermite series (van der Marel & Franx 1993) and the solution is based on the maximum penalised likelihood formalism (see Cappellari & Emsellem 2004 and references therein for details). The engineering grade detector used in SINFONI during the time of the observations had a large dead region at the red end of the spectrum, which compromised the data quality in the K -band beyond $>2.4 \mu\text{m}$. Therefore, only the H -band was used. The fitting was done using only the low-order moments (v, σ), as including the higher orders h_3 and h_4 did not provide a significant improvement in the quality of the fit, most likely due to relatively low S/N and beam-smearing. Late type stars (K3V, M0V, M5III) obtained with SINFONI for another observing program were used as templates.

We derive $\sigma = 210 \pm 20 \text{ km s}^{-1}$, in agreement with $\sigma = 175 \pm 24 \text{ km s}^{-1}$ of Dasyra et al. (2006) and $188 \pm 10 \text{ km s}^{-1}$ of Tacconi et al. (2002). The H -band continuum is consistent with late type stellar template, with no need to introduce a non-stellar component to the fit. This is in contrast to the findings of Vanzi et al. (2002), according to whom the non-stellar component contributed 30 percent of the H -band emission based on a similar fitting on the H -band and an even higher fraction based on broad-band colours.

The disappearance of the non-stellar component is not surprising as our observations and those of Vanzi et al. were separated by 5 years. The most likely origin of the diluting continuum is hot dust heated close to the sublimation temperature, and therefore follows closely changes in the heating flux. Alternatively, the diluting continuum may be due to synchrotron, as has been suggested for some of the nearby AGN in near-IR (Prieto et al., in preparation). In both cases the implication is that, at least in near-IR, the non-stellar continuum is solely due to the AGN. As discussed above, the Super-antennae may be AGN dominated even in mid-IR (Charmandaris et al. 2002; Risaliti et al. 2003; 2006).

3.4 Emission line morphologies

The emission line fluxes relative to the nuclear peak flux, the full width at half-maximum (FWHM) of the Gaussian fitted to the line profile and the velocity field for Pa α 1.87 μm , [Fe II] 1.64 μm and the H₂ line 1–0 S(1) 2.12 μm are displayed in Fig. 4. For comparison, the HST 0.8 μm image mildly smoothed to 0.3 resolution is shown in contours. The alignment between the HST image and SINFONI data

was based on the position of the nuclear continuum source. While the southern nucleus is red, and the optical nucleus may therefore not coincide with the near-IR nucleus, no evidence for this is found based on comparison between large-field near-IR and HST images, at least within the seeing-limited resolution of data discussed in this paper. In case of Pa α , the continuum wavelength range in automatic line fitting has been selected to exclude contribution from “broad” component; thus the fitting procedure (and line ratios) is comparable with the other lines where the Pa α components cannot be detected.

As the SINFONI field of view does not contain any stars, a direct estimate for the achieved spatial resolution cannot be derived based on the data itself. Furthermore, the DIMM sensor measures optical seeing close to zenith while the Super-antennae was observed at an airmass of ~ 1.5 . The nucleus is unresolved in the K -band image (Vanzi et al.), where the spatial resolution $\sim 1''.0$ (1.3 kpc) can be derived directly from the numerous stars present in the large f.o.v. After collapsing the spectral cubes in emission line-free wavelengths, we derive the FWHM size for the nuclear continuum source 0.9 both in H and K , similar to that measured from pure emission line maps for the main emission lines (Pa α , [Fe II], H₂ lines). While these values are larger than reported by the DIMM in the optical, especially during H -band observations, the derived nuclear sizes are inconsistent with the unresolved nucleus in broadband images. More likely, the DIMM sensor has underestimated the optical seeing and the nucleus is unresolved in both the collapsed spectral continuum images and emission lines.

While the nuclear source itself is unresolved, a fainter extended component can be detected in most emission lines. The most extended emission line is Pa α 1.8756 μm , which is dominated by the nucleus with spiral structures extending to south-east and north-west. These Pa α features coincide with the dusty spiral present in HST archive images (Fig. 1). Similar to H α emission (Mihos & Bothun 1998), both Pa α and molecular H₂ lines show enhanced emission northwest of the nucleus. The southern spiral consisting of several clumps (starforming regions) is also faintly traced in H₂. Furthermore, a separate starforming clump is seen only in Pa α $\sim 3''$ north of the nucleus coinciding with the bridge detected in continuum (Fig. 1) connecting the southern galaxy to the northern.

3.5 Molecular gas

Davies et al. (2003) studied the molecular gas in 7 ULIRGS and found that while the 1–0 transitions appear to be thermalised, the same is not true for 2–1 and 3–2 transitions. They concluded the H₂ excitation is predominantly UV fluorescence, but the lower levels are thermalised by intermolecule collisions in dense clouds. This produces different excitation temperatures, $\sim 1300 \text{ K}$ based on $v = 1$ transitions and $\sim 5000\text{--}6000 \text{ K}$ based on $v = 2$ and $v = 3$ transitions. In order to probe the fainter transitions, we have corrected the spectra for rotation with velocities derived from the 1–0 S(1) line. This “derotation” increases S/N of the spectra by decreasing the width of the spectra features and decorrelates possible telluric residuals; this procedure is identical to what was used in Davies et al. (2005). However, due to a lack of CO-bandheads at K -band, the template fitting is so

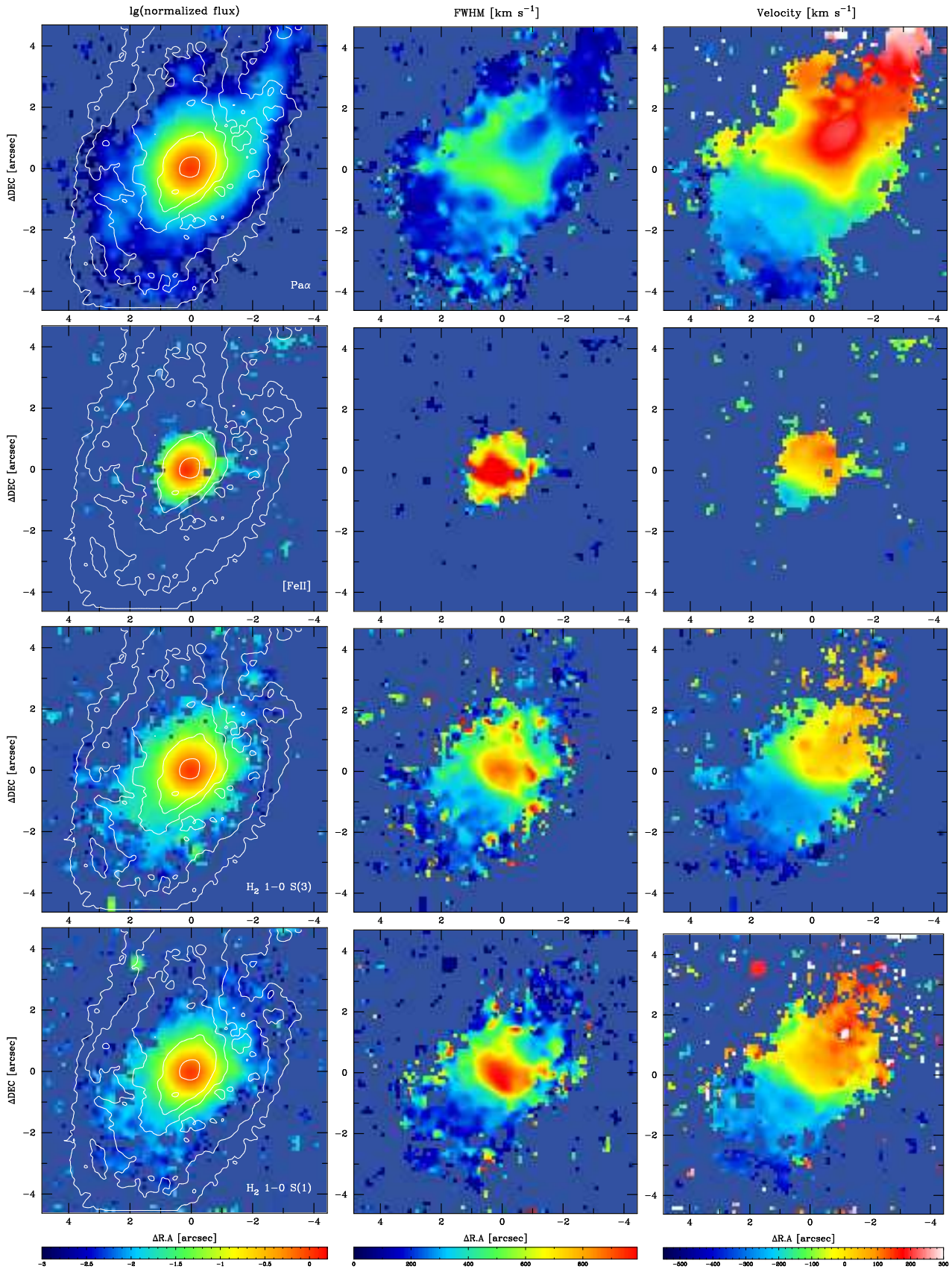


Figure 4. From left to right, the flux normalised to the peak nuclear flux, Gaussian FWHM and the velocity field for Pa α (top row; excluding the “broad” component), [FeII] (middle row) and H₂ 1–0 S(1) (bottom row). The optical morphology from HST 0.8 μ m image is shown in contours.

Table 2. Comparison between the H₂ emission line ratios in ULIRGs, AGN and the Super-antennae; the Br γ for the extended case is estimated from Pa α

Line	ULIRG	AGN	Super-antennae	
			Nucleus	Extended
1-0 S(3)	0.595	0.739
1-0 S(2)	0.337 \pm 0.018	0.379 \pm 0.068	0.496	0.327
2-1 S(3)	0.146 \pm 0.022	0.217 \pm 0.132	0.045	0.045
1-0 S(1)	1.000	1.000	1.000	1.000
2-1 S(2)	0.074 \pm 0.007	0.118 \pm 0.012	0.039	< 0.06
1-0 S(0)	0.271 \pm 0.035	0.327 \pm 0.047	0.308	0.350
2-1 S(1)	0.142 \pm 0.031	0.125 \pm 0.038
Br γ	0.6-1.33		0.256	0.164

badly constrained, that we are unable to remove the stellar contribution.

The comparison between the average line ratios presented by Davies et al. (2003) for ULIRGS, Davies et al. (2006) for AGN and the Super-antennae is presented in Table 2. For the Super-antennae, the line ratios both for the nuclear region ($r < 0''.6$) and extended emission ($1''.25 < r < 2''.5$) are given. When compared with the ULIRG sample, the 2-1 transitions appear weaker both at the nucleus and in the extended annulus, and are not overpopulated relative to the 1-0 transitions. Br γ /1-0S (1) is much lower at the nucleus, and in the extended annulus Br γ cannot be even detected. Assuming the Case B Pa α /Br γ ratio of 12.1, we infer a Br γ /1-0 S(1) ratio of ~ 0.16 there. The decrease in Pa α /1-0 S(3) ratio is also clearly visible in Fig. 6, which interestingly also reveals a small ring-like structure with diameter $\sim 1''.5$.

We have estimated the excitation temperature from 1-0 S(3)/1-0 S(1), and ortho/para ratio from 1-0 S(2)/1-0 S(1) since these are the strongest H₂ emission lines in the spectra. The ortho/para ratio can easily be shown to be practically independent of extinction:

$$f_{o/p} = \frac{1.1102 [S(3)/S(1)]^{0.449}}{S(2)/S(1)} 10^{-0.004 A_K}, \quad (1)$$

where $S(x)$ denotes the observed intensities for 1-0 S(x) emission lines and A_K is the K -band extinction assuming $A_\lambda \propto \lambda^{-1.85}$ and the A -coefficients from Wolniewicz, Simbotin & Dalgarno (1998). The ortho/para map is shown in Fig. 5, showing a relatively constant ratio. By summing the “derotated” spectra in annuli, we can follow the ortho/para ratio changes further out than calculating it in individual spectra. At the nucleus ($r < 0''.6$) the ratio is 2.4 ± 0.1 , and remains similar in the annulus $0.6 < r < 1.25''$. Further out, the ratios are consistent with thermal excitation of H₂ (ortho/para ~ 3). As the minimum values detected in ortho/para ratio coincide with the ring-like structure visible in Pa α /1-0 S(3) ratio, it is likely that in the nuclear region H₂ is excited by UV fluorescence in dense clouds. A contribution from X-ray excitation may be needed to depopulate the 2-1 states (e.g. Gredel & Dalgarno 1995), as Davies et al. (2003) observed larger ratios in their ULIRG sample. Similar scenario has been suggested for NGC 6240 (Draine & Woods 1990), though higher-resolution data is clearly needed to properly resolve the possible starbursting ring and separate the mechanisms.

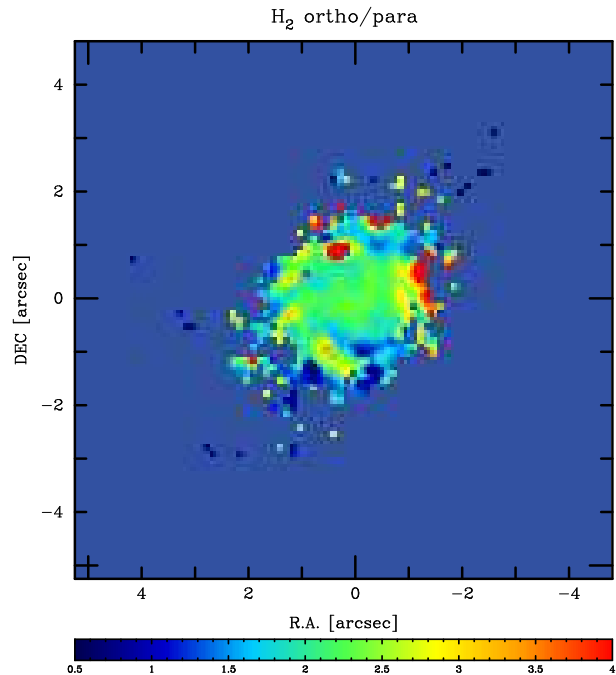


Figure 5. Ortho-Para ratio of H₂ determined from 1-0 lines S(1), S(2), S(3)

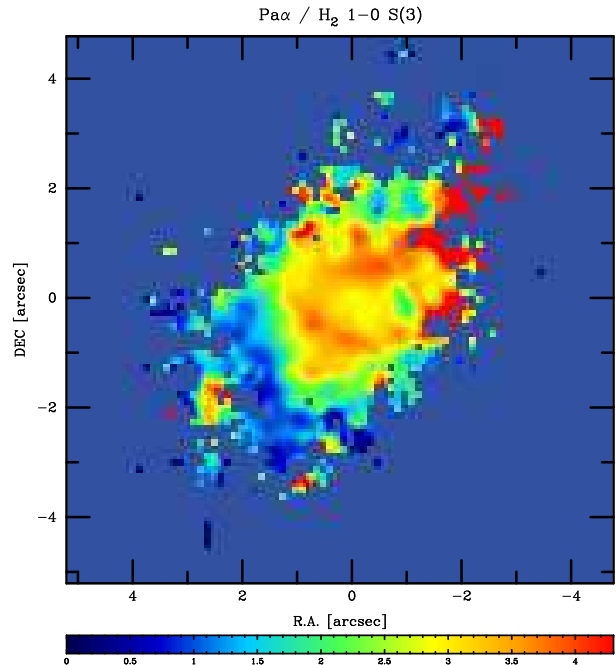


Figure 6. The Pa α /H₂ 1-0 S(3) ratio

For the extended H₂ gas the situation is more clear, as both the ortho-para ratio and low Pa α /H₂ line ratio suggest thermal excitation through shocks. While in principle X-rays can also produce low Pa α /H₂ ratios (Gredel & Dalgarno 1995), such a scenario seems unlikely, as the likely origin for the extended X-ray emission is supernovae; however, [Fe II] is strongly concentrated at the nuclear region.

The average column density of molecular hydrogen within the 5×5 pixel region is $1.8 \times 10^{18} \text{ cm}^{-2}$, correspond-

ing to the total mass of hot excited molecular hydrogen of $1.8 \times 10^4 M_{\odot}$. The peak (seeing dependent) column density is a factor of 1.3 bigger than the average value. The total mass of the available molecular material as determined from CO radio emission is several orders of magnitudes larger, $3 \times 10^{10} M_{\odot}$ (Mirabel et al. 1990); however, the radio beamsize ($44''$) includes both the nuclei in the system.

3.6 Kinematics

Low resolution H α velocity maps for the Super-antennae were presented by Mihos & Bothun (1998), whose Fabry-Perot images also covered the northern galaxy. The most notable difference between our maps and theirs is the plume detected in H α in East of the nucleus, which is not very extended in Pa α . This may be simply due to lower signal to noise ratio at the outer edges of the mosaiced spectra. The faint streaming motion with $\Delta v \simeq -130 \text{ km}^{-1}$ appears to be present in Pa α in South of the nucleus extending up to $4''$ (Fig. 4).

We have applied the Kinemetry IDL routine described by Krajnović et al. (2006) to the data. This method is a generalisation of surface photometry performed in isophotal annuli of galaxies applied to higher order moments (v , σ , h_3 , h_4 ...). The routine can either use a constant systemic velocity or allow it to change as a function of radius; for isolated, non-interacting galaxies the systemic velocity (A_0 following the terminology in Krajnović et al. 2006) is expected to be nearly constant. We have tried both methods with Pa α in the Super-antennae, but constant A_0 produces a poorer match with the observed velocity field. The parameters of the warped disk model with A_0 kept as a free parameter are shown in Fig. 7. For the four innermost radii, the fitting is done inside the PSF and therefore the position angle and ellipticity have very large errors. This simply represents the fact that while the fitting process is numerically stable even inside the HWHM radius of the PSF, the shape parameters derived there have no real physical meaning.

The fitting has revealed the presence of at least two separate kinematic components within the central $r = 4''$ in the Super-antennae, possibly three. In the inner parts of the galaxy the velocity field is well modelled by a warped disk model, and the residuals between the observed velocities and model are generally within $\sim 25 \text{ km s}^{-1}$. Northeast and west of the nucleus, the residuals are much larger, up to 150 km s^{-1} . While the shape parameters (q and position angle) of the *outermost* ellipses does depend on how large the area the fitting is carried out over or whether the beginning of the spirals arms is included or not, the closeness of the edge of usable data does not affect these residuals significantly. Especially northeast of the nucleus, the area of large residuals is also clearly visible in the observed velocity field (Fig. 4).

The ellipticity of the fitted rings, related to the flattening parameter of Krajnović et al. (2006) by $q = 1 - \epsilon$, gradually increases from 0.24 at $r = 0''.68$ to 0.45 at $r > 2''$, while the position angles of the ellipses are almost constant, $327\text{--}331^\circ$. A_0 represents the systemic velocity of the fitted ellipses and is relatively stable between $0''.8 - 2''$, $\sim 18530 \text{ km s}^{-1}$. Further out, A_0 decreases and the ratio k_5 increases. As the presence of multiple components is detected by the rise of the k_5 coefficient in parametrisation of Krajnović et

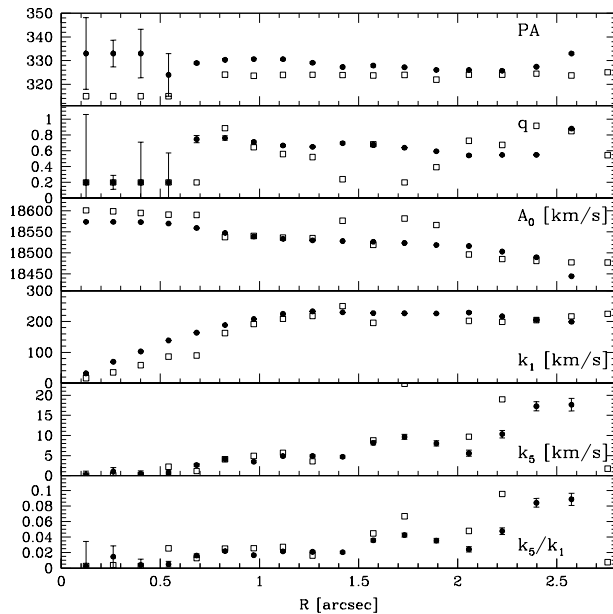


Figure 7. Kinematic model parameters for the Pa α emission (circles with error bars) and H $_2$ 1–0 S(1) (open squares). From top to bottom: the position angle of the ellipses, the flattening coefficient q (related to ϵ by $q = 1 - \epsilon$), the systemic velocity A_0 , rotational velocity k_1 and non-rotational velocity component k_5 .

al. (2006), this indicates that the outer parts of the galaxy do not follow the same disk-like kinematics as the inner parts. This outer component is already clearly visible in the observed velocity field (Fig. 4). Further support for the separate outer component comes from the Gauss-Hermite expansion of the Pa α profile (Fig. 8), where the higher order moments h_3 and h_4 are directly observable quantities without any modelling assumptions. h_3 and h_4 in the inner regions closely follow the expectations for a warped disk located at position angle of $\sim 330^\circ$. Northeast and west of the nucleus, both h_3 and h_4 show significant deviations from disk-like rotation; these deviations coincide with the the regions with $v_{obs} - v_{model} < -25 \text{ km s}^{-1}$ of the model fitting.

Closer still to the nucleus, with $r < 0''.7$, the fitted A_0 values are higher than in the surrounding region. The nature of this jump is not clear based on the current, seeing limited data. The redshifted nuclear velocities appear to be connected with the positive residuals present in $v_{obs} - v_{model}$ map at position angle of $\sim 70^\circ$ (Fig. 8).

We have repeated an identical fitting procedure with 1–0 S(1) as we did with Pa α . Overall, the quality of the kinematic fitting on 1–0 S(1) is limited both by lower S/N and smaller spatial extent of the data. The most notable differences between the velocity field of molecular gas and ionized medium is that the 1–0 S(1) is redshifted by 80 km s^{-1} relative to Pa α at the nucleus and blueshifted by $\sim 90 \text{ km s}^{-1}$ in the Northwest. Despite these differences, the H $_2$ velocity field is consistent with rotating disk with similar kinematic parameters than derived for Pa α (Fig. 7). Relatively large $v_{obs} - v_{model}$ residuals upto $\sim 100 \text{ km s}^{-1}$ are detected Northwest of the nucleus coinciding with the region where 1–0 S(1) is blueshifted relative to Pa α (Fig. 8). Interestingly, 1–0 S(3) velocity field is significantly different

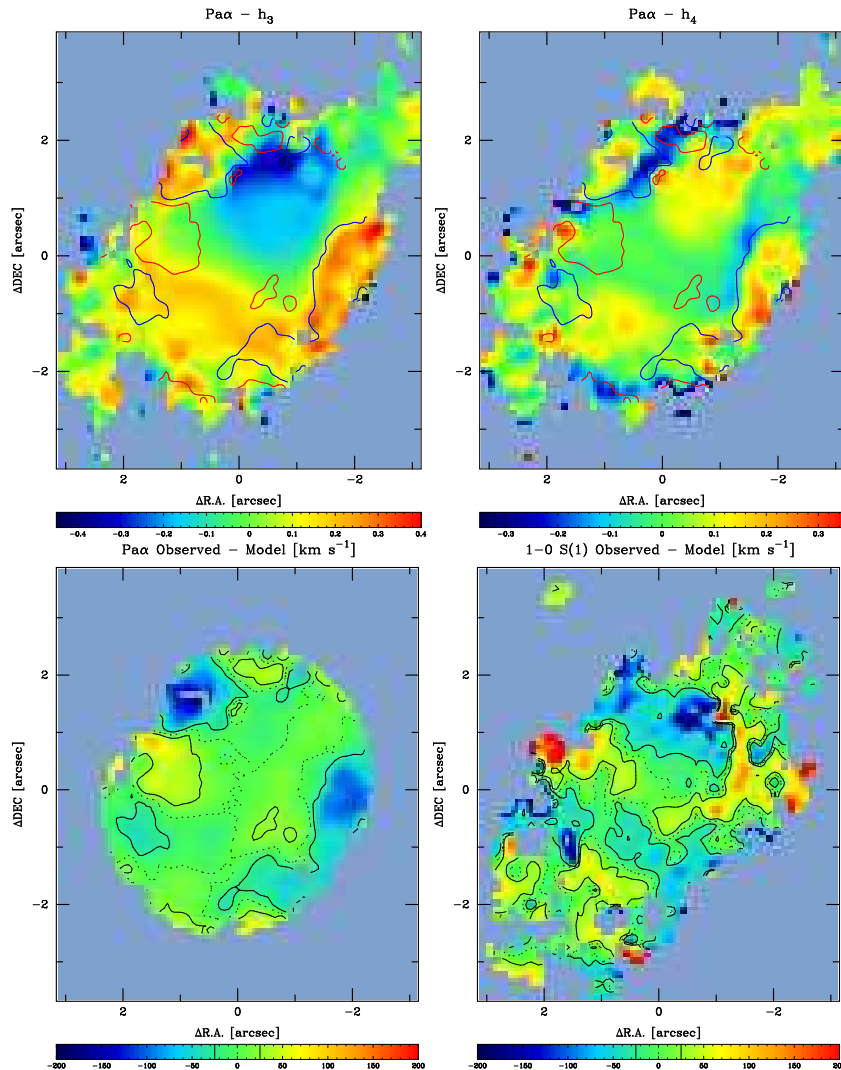


Figure 8. Kinematic model of Pa α and 1–0 S(1) emission in the Super-antennae. The h_3 and h_4 components from Gauss-Hermite expansion of the Pa α profile are shown *upper left* and *upper right*, respectively. The difference between v_{obs} and v_{model} constructed without including higher order harmonics (rotation only) is shown for Pa α (*lower left*) and 1–0 S(1) (*lower right*). The contours in h_3 and h_4 figures show the Pa α regions with $v_{obs} - v_{model} = \pm 25$ km s $^{-1}$.

from 1–0 S(1) northwest of the nucleus. The blue component of S(3) emission line is stronger than in S(1); thus the excitation temperature of the blue component is higher. This difference is unlikely to be due to extinction, as the wavelength difference between the lines is relatively small and therefore they both suffer from similar amounts of reddening.

4 CONCLUSIONS

We have presented the results of near-IR integral field spectroscopy of the southern galaxy of the Super-antennae. The main results obtained from this project are:

- Pa α arises in a warped disc with position angle of $\sim 330^\circ$ and inclination $i=40\text{--}55^\circ$. The kinematic parameters derived for H $_2$ are similar.

- Unlike in previous studies, we found the H-band continuum to be consistent with pure stellar emission, with no evidence for diluting non-stellar continuum at present.

- The Pa α /H $_2$ line ratio maps reveal the presence of the ring-like structure with diameter $\sim 1.5\text{--}2.0''$, coinciding the the region with lowest H $_2$ ortho/para ratios. This morphological argument together with non-thermal ortho-para ratios suggest UV fluorescence in dense clouds is an important H $_2$ excitation mechanism in the nuclear region.

- Extended H $_2$ emission with $r > 1''.3$ has thermal ortho/para ratio and very low Pa α /H $_2$ line ratios, indicating that thermal excitation in shocks is important at larger radii.

5 ACKNOWLEDGEMENTS

We thank Leonardo Vanzi for kindly providing us the broadband images and Richard McDermid for fruitful discussion during the work. We are grateful to Davor Krajnović

and Michele Cappellari for making their software publicly available. This work is based on observations collected at the European Southern Observatory, Paranal, Chile, (60.A-9041(A)). This research has made use of the NASA/IPAC Extragalactic Database (NED) which is operated by the Jet Propulsion Laboratory, California Institute of Technology, under contract with the National Aeronautics and Space Administration.

REFERENCES

- Berta S., Fritz J., Franceschini A., Bressan A., Pernechele C., 2003, *A&A*, 403, 119
- Black J. H., van Dishoeck E. F., 1987, *ApJ*, 322, 412
- Blietz M., Cameron M., Drapatz S., Genzel R., Krabbe A., van der Werf P., Sternberg A., Ward M., 1994, *ApJ*, 421, 92
- Bonnet H., et al., 2004, *Msngr*, 117, 17
- Braito V., et al., 2003, *A&A*, 398, 107
- Cappellari M., Emsellem E., 2004, *PASP*, 116, 138
- Charmandaris V., et al., 2002, *A&A*, 391, 429
- Colina L., Lipari S., Macchetto F., 1991, *ApJ*, 379, 113
- Contini M., Viegas S. M., 2001, *ApJS*, 137, 75
- Dasyra K. M., et al., 2006, *ApJ*, 638, 745
- Davies R. I., Sternberg A., Lehnert M., Tacconi-Garman L. E., 2003, *ApJ*, 597, 907
- Davies R. I., Sternberg A., Lehnert M. D., Tacconi-Garman L. E., 2005, *ApJ*, 633, 105
- Dennefeld M., 1986, *A&A*, 157, 267
- Draine B., Woods D. T., 1990, *ApJ*, 363, 464
- Duc P.-A., Mirabel I. F., Maza J., 1997, *A&AS*, 124, 533
- Eisenhauer F., et al., 2003, *SPIE*, 4841, 1548
- Farrah D., Afonso J., Efstathiou A., Rowan-Robinson M., Fox M., Clements D., 2003, *MNRAS*, 343, 585
- Genzel R., et al., 1998, *ApJ*, 498, 579
- Gerhard O. E., 1993, *MNRAS*, 265, 213
- Goldader J. D., Joseph R. D., Doyon R., Sanders D. B., 1997, *ApJS*, 108, 449
- Gredel R., Dalgarno A., 1995, *ApJ*, 446, 852
- Halpern J. P., Oke J. B., 1986, *ApJ*, 301, 753
- Hollenbach D., McKee C. F., 1989, *ApJ*, 342, 306
- Krajinović D., Cappellari M., de Zeeuw P. T., Copin Y., 2006, *MNRAS*, 366, 787
- Maiolino R., Krabbe A., Thatte N., Genzel R., 1998, *ApJ*, 493, 650
- Marconi A., Moorwood A. F. M., Salvati M., Oliva E., 1994, *A&A*, 291, 18
- Mihos J. C., Bothun G. D., 1998, *ApJ*, 500, 619
- Mirabel I. F., Lutz D., Maza J., 1991, *A&A*, 243, 367
- Mirabel I. F., Booth R. S., Johansson L. E. B., Garay, G., Sanders, D. B., 1990, *A&A*, 236, 327
- Murphy T. W., Jr., Soifer B. T., Matthews K., Armus L., Kiger J. R., 2001, *AJ*, 121, 97
- Osterbrock D. E., Tran H. D., Veilleux S., 1992, *ApJ*, 389, 305
- Pappa A., Georgantopoulos I., Stewart G. C. 2000, *MNRAS*, 314, 589
- Pernechele C., Berta S., Marconi A., Bonoli C., Bressan A., Franceschini A., Fritz J., Giro E., 2003, *MNRAS*, 338, L13
- Reunanen J., Kotilainen J. K., Prieto M. A., 2003, *MNRAS*, 343, 192
- Risaliti G., et al., 2003, *ApJ*, 595, L17
- Risaliti G., et al., 2006, *MNRAS*, 365, 303
- Rodríguez-Ardila A., Viegas S. M., Pastoriza M. G., Prato L., 2002, *ApJ*, 579, 214
- Schreiber J., Thatte N., Eisenhauer F., Tecza M., Abuter R., Horrobin M., 2004, *ASPC*, 314 380
- Spergel D. N., et al., 2003, *ApJS*, 148, 175
- Sternberg A., Dalgarno A., 1989, *ApJ*, 338, 197
- Tacconi L. J., et al., 2002, *ApJ*, 580, 73
- Tran H. D., 2003, *ApJ*, 583, 632
- van der Marel R., Franx M., 1993, *ApJ*, 407, 525
- Vanzi L., Bagnulo S., Le Floch E., Maiolino R., Pompei E., Walsh W., 2002, *A&A*, 386, 464
- Wolniewicz L., Simbotin I., Dalgarno A., 1998, *ApJS*, 115, 293